Nanoscale

Ta-Doped Porous TiO2 Nanorods Arrays by Substrate-Assisted Synthesis: Efficient Photoelectrocatalysts for Water Oxidation

Journal:	*Nanoscale*
Manuscript ID	NR-ART-05-2018-004003.R1
Article Type:	Paper
Date Submitted by the Author:	18-Aug-2018
Complete List of Authors:	He, Shiman; Sun Yat-sen (Zhongshan) University, School of Chemistry and Chemical Engineering Meng, Yuying; Sun Yat-Sen University, Wu, Qili; Sun Yat-sen University, Yang, Jingling; Sun Yat-Sen University, MOE Key Laboratory of Bioinorganic and Synthetic Chemistry, School of Chemistry Huang, Senchuan; MOE Laboratory of Bioinorganic and Synthetic Chemistry, School of Chemistry and Chemical Engineering Li, Xiaohui; Sun Yat-Sen University, School of Chemistry Tong, Shengfu; Sun Yat-Sen University, School of Chemistry and Chemical Engineering Asefa, Tewodros ; Rutgers, The State University of New Jersey, b. Department of Chemistry and Chemical Biology and Department of Chemical and Biochemical Engineering Wu, Mingmei; Sun Yat-sen (Zhongshan) University, School of Chemistry

Journal Name

ARTICLE

ROYAL SOCIETY
OF CHEMISTRY

Ta-Doped Porous TiO₂ Nanorods Arrays by Substrate-Assisted Synthesis: Efficient Photoelectrocatalysts for Water Oxidation

Shiman He,[a] Yuying Meng,*[a] Qili Wu,[a] Jingling Yang,[a] Senchuan Huang,[a] Xiaohui Li,[a] Shengfu Tong,[a] Tewodros Asefa,*[b] and Mingmei Wu*[a]

Owing to its excellent chemical stability and low cost, titanium dioxide (TiO₂) has been widely studied as photoanode for photoelectrochemical (PEC) water splitting. However, TiO₂'s practical applications in solar energy-to-synthetic fuel conversion processes has been constrained by its inherently poor ability to transport photogenerated electrons and holes. In this paper, we report Ta-doped porous TiO₂ nanorods arrays on Ta foil (Ta-PTNA) that do not possess this issue and that can thus efficiently photoelectrocatalyze water oxidation, helping the production of H₂ (a clean fuel) from water at the expense of solar light. The materials are synthesized by a new, facile synthetic approach involving hydrothermal treatment of a TiO₂ precursor with Ta foil, without seeds and templates, and followed by calcination of the product. Besides serving as a source of Ta dopant atoms, Ta foil is found to play a vital role in the formation of nanopores in the materials. The material obtained with hydrothermal treatment at 180 °C for 10 h (Ta-PTNA-10), in particular, affords very large photocurrent density and very high photoconversion efficiency (0.32 % at 0.79 V vs. RHE, which is better than those of many previously reported photocatalysts and ~4 times larger than that of undoped TiO₂ nanorods arrays). Ta-PTNAs' remarkable PEC catalytic performance is found to be due to their nanoporous structure and high electronic conductivity.

1. Introduction

The development of alternative, environmentally-friendly energy systems has become critical as the consumption of fossil fuels reserves (petroleum, natural gas, coal, etc.) remain unabated and fossil fuels' ongoing negative environmental impacts (*e.g.*, water, soil and air pollution) are growing.[1, 2] These include renewable, clean, carbon-free energy carriers such as dihydrogen (H₂), which can reduce and/or eliminate our over-reliance on fossil fuels.[3, 4] Photoelectrochemical (PEC) water splitting, where electrolysis of water is driven by sunlight using semiconductor materials as catalysts or photoanodes, is one of the most appealing, sustainable and promising technologies to produce H₂.[5] Among various metal oxide semiconductor materials being investigated as photoelectrodes for water splitting, TiO₂ has attracted substantial attention ever since the report of PEC water splitting over TiO₂ by Fujishima and Honda in 1972.[6] However, the intrinsic low electron mobility (1 cm² V⁻¹ s⁻¹) and the short minority carrier (hole) diffusion length (10 - 100 nm) in TiO₂ greatly diminish TiO₂'s photo-to-current conversion efficiency, even under UV irradiation.[7] It has been reported that the rate of photoconversion of light to current on TiO₂ can be improved by making TiO₂ with nanoscale sizes as well as by tuning its structure and morphology.[8-10]

Hence, various nanostructured TiO₂ electrodes, especially with one-dimensional (1-D) structure, have been synthesized and studied.[11, 12] Such materials (especially TiO₂ nanowires and nanorods) can attain relatively high solar energy conversion efficiency or photocatalytic performance for water splitting due to their relatively short diffusion pathways for photogenerated holes.[13-15] Furthermore, by introducing nanoporous structure in TiO₂ photoanodes, larger contact area between the material and electrolyte, better electron transport, improved light harvesting and greater charge separation efficiency can be achieved in them.[16-18] Another approach that has proven effective to increase the catalytic performance of TiO₂ photoelectrodes is the incorporation of metal dopants such as Ta into the material.[19-21] Among various metal dopants, Ta can be easily incorporated into TiO₂ lattice without causing large distortion due to the similar atomic radius of Ta and Ti elements.[22, 23] Besides, rutile TiO₂ can epitaxially grow on Ta metal substrate because of their perfect crystalline structures match, giving the enhanced combination between TiO₂ and Ta substrate.[24] Given these, we had hypothesized that the PEC catalytic performance of TiO₂ can be significantly boosted by making it to have all these three features at the same time, namely, 1-D nano-architecture, metallic dopants as well as nanoporous structures.

To this end, we here report the synthesis of densely grown, nanoporous Ta-doped TiO₂ nanorod (1-D) arrays on Ta foil (denoted Ta-PTNA materials) that can serve as efficient PEC

a. MOE Key Laboratory of Bioinorganic and Synthetic Chemistry, School of Chemistry, Sun Yat-Sen University, No. 135, Xingang Xi Road, Guangzhou 510275, P. R. China.

b. Department of Chemistry and Chemical Biology and Department of Chemical and Biochemical Engineering, Rutgers, The State University of New Jersey 610 Taylor Road, Piscataway, New Jersey 08854, USA.

catalysts for water oxidation (Figure 1a). The synthesis involves a facile two-step procedure comprising hydrothermal treatment of a TiO$_2$ precursor with Ta foil without any template or capping agents, followed by calcination of the product (see Table S1 and details in Experimental Section below). The porous structures in the nanorods seem to have formed by Ta-assisted Kirkendall effect, a process that has never before been reported for 1-D TiO$_2$.[24, 25] Besides serving as a substrate, the Ta foil delivers dopants by undergoing dissolution in the HCl solution used for the synthesis and then providing Ta^{5+} ions to be incorporated into the cube-shaped TiO$_2$ (rutile) seeds and subsequently to the nanorods growing over the seeds. Finally, pores form in each nanorod of Ta-doped TiO$_2$ nanorods arrays during a calcination step. The resulting Ta-PTNA materials show high photocatalytic activity for PEC water oxidation compared with many other photocatalysts and the undoped TiO$_2$ nanorods prepared on FTO (named undoped TiO$_2$/FTO) as control materials for comparative studies.

2. Experimental Section

Synthesis of Ta-PTNA Materials

First, Ta foils were cut into small pieces with sizes of *ca*. 1.5 cm × 2.0 cm. The small pieces of Ti foils were then cleaned in 2-propanol, then acetone, and finally deionized water under sonication (for 30 min each) at room temperature. The Ta foils were further treated with 2 M NaOH solution at 55 °C under sonication for 30 min to remove any tantalum oxide present on their surfaces. After rinsing the solution completely, they were dried in a vacuum oven at 60 °C for 12 h. They then became ready for growing the Ta-doped nanoporous TiO$_2$ nanorods arrays on them under different conditions as compiled in Table S1.

For the synthesis of the series of the desired materials, six 15 mL-sized Teflon-lined stainless-steel autoclaves were taken, and into each one of them 5 mL of deionized water was mixed with 5 mL of concentrated HCl solution. After stirring under ambient condition for 5 min, into each autoclave 0.20 mL of tetrabutyl titanate was gradually added using a pipette. The solutions were kept stirring for another 15 min, after which a cleaned Ta foil prepared above was placed inside each solution at an angle of 45 ° against the wall of the Teflon-liner. The autoclaves were then immediately kept in an electric oven and the samples were subjected to hydrothermal treatment at 180 °C for variable periods of time, namely 1, 3, 5, 10, 15 or 24 h. After letting them cool to room temperature, the substrates were taken out of the autoclaves, washed thoroughly with deionized water and allowed to dry under ambient condition. Finally, the as-obtained samples were calcined at 450 °C for 1 h at a heating rate of 5 °C min^{-1}. The products were named as Ta-PTNA-*t* (where *t* represents the hydrothermal time) (see Table S1).

In addition, a series of control materials (A series) was synthesized by treating the precursors hydrothermally at temperatures of 160 and 200 °C (instead of at 180 °C) for 10 h, followed by calcination at 450 °C for 1 h. A second series of control materials (B series) was obtained by calcining the

products obtained hydrothermally at 180 °C for 10 h at different calcination temperatures, namely 250, 300, 350, 400, 500 and 550 °C for 1 h. A third and last series of control materials (C series) was obtained by making the material hydrothermally at 180 °C for 10 h and then calcining the product at 450 °C for different times, *i.e.* 0, 30 or 120 min. The different synthetic parameters/conditions are all compiled in Table S1 below.

For comparison, undoped TiO$_2$ nanorods were synthesized using fluorine-doped tin oxide (FTO) as a substrate hydrothermally at 180 °C for 10 h and then calcining the product at 450 °C for 1 h. This product was named as undoped TiO$_2$/FTO.

Preparation of Undoped TiO$_2$ Nanorods Coated on Ta Foil and FTO Substrates

Undoped TiO$_2$ nanorods on Ta foil and FTO substrates were synthesized by drop-coating method. In detail, 6 mg of undoped TiO$_2$ powder was obtained from TiO$_2$/FTO by scrapping off the FTO slide. It was then dispersed in *N,N*-dimethylformamide (600 μL) under sonication for 1 h. Then, 20 μL of the resulting suspension of TiO$_2$ nanorods was drop-coated on Ta foil or FTO substrate, and the slides were dried at 60 °C for 30 min. This procedure was repeated 3 times. The materials were then kept at 60 °C for 4 h to dry. Finally, the films were annealed at 450 °C for 1 h.

Instrumentation and Materials Characterization

Various techniques were used to systemically characterize the as-prepared materials. The crystallographic phase(s) were determined by powder X-ray diffraction (XRD) using a Rigaku D/max diffractometer operating with a Cu *Kα* source (λ = 1.5406 Å). The XRD patterns were obtained in a 2ϑ range from 20 ° to 80 ° at a scan rate of 10 ° min^{-1}. High resolution XRD patterns were obtained at a scan rate of 0.12 ° min^{-1} for the TiO$_2$ sample obtained from Ta foil by scraping and then placed on a Si slide. The Rietveld analysis was performed with the refinement program Topas 3.0. The morphology and microstructure of the materials were characterized using scanning electron microscope (FEI Quanta 400) equipped with an energy-dispersive X-ray spectroscopy (EDX) and operated at an accelerating voltage of 20 kV. Transmission electron microscopy (TEM) and scanning transmission electron microscopy (STEM) images were collected using transmission electron microscope (FEI Tecnai G2 F30) equipped with a high angle annular dark field (HAADF) detector with an accelerating voltage of 300 kV. The absorption spectra of TiO$_2$ film were measured with UV-Vis-NIR spectrophotometer (Shimadzu UV-3600) using BaSO$_4$ as a reference. X-ray photoelectron spectra and data were acquired with X-ray photoelectron spectrometer (XPS) (ESCALab250) operating with a monochromatic X-ray source (Al *Kα*). The binding energies were calibrated using the C 1s peak at 284.8 eV. The energy resolution for the survey and the high-resolution scans were performed with 1 and 0.1 eV, respectively. The photoluminescence (PL) spectra were recorded on an

Edinburgh Instruments FLS 920 with an excitation wavelength of 340 nm. Time-resolved photoluminescence (TRPL) spectra were recorded on an Edinburgh Instruments FLS 920 fluorimeter with excitation and detection wavelength at 340 nm and 410 nm, respectively.

Photoelectrochemical Analysis and Photocatalytic Tests

The photocurrent density (J_p) over TiO_2 was evaluated in 0.2 M Na_2SO_4 aqueous solution (pH 7.04) at 50 mV s^{-1} using a typical three-electrode configuration comprising TiO_2 electrode, Ag/AgCl electrode and Pt mesh as the working, the reference and the counter electrodes, respectively. The potential was controlled by a Metrohm Auto Lab (PGSTAT302N). The photoresponse was measured under chopped irradiation from 300 W Xe lamp (Perfect light PLS-SXE300CUV) equipped with an AM1.5G filter, calibrated with a standard Si solar cell to simulate AM 1.5G illumination (100 mW cm^{-2}). The photoconversion efficiency of the material depends on the applied potential. The applied bias photon-to-current efficiency (ABPE, %) was calculated from the *I-V* curves using the equation: ABPE = I (1.23 − E) / J_{Light}, where I is the photocurrent density, E is the applied voltage *vs.* RHE, and J_{light} is the irradiance intensity of 100 mW cm^{-2} (AM 1.5G).[26] The incident photon-to-current conversion efficiencies (IPCE) is expressed as IPCE = (1240 I) / ($\lambda \cdot P_{light}$), where I is the photocurrent density, λ is the incident light wavelength, and P_{light} is the power density of monochromatic light at a specific wavelength of irradiated light.[27] The evolved gases were detected using a gas chromatograph (Agilent GC 7820A).

Electron flux, number of electrons (Ne), of AM1.5G solar spectrum was calculated from solar spectral irradiance using the equation: $N_e = E \cdot e \cdot [(\lambda \cdot 10^{-9}) / (h \cdot c)]$, where e is the charge of electron (1.6022 × 10^{-19} C), h is the Planck constant (6.626 × 10^{-34} J·s), and c is the speed of light (2.9979 × 10^8 m s^{-1}). In addition, the electron flux of photoanode could be obtained from the product of the AM1.5G electron flux, $N_e \times \eta_{LHE}$. Photocurrent density (J_{Abs}) under 100 % absorbed photon conversion efficiency was determined by integrating the electron flux at the photoanodes across 300 - 420 nm wavelength range.[28] The charge injection efficiency ($\eta_{Injection}$) and separation efficiency ($\eta_{Separation}$) were estimated as functions of applied potential by using 0.5 M potassium phosphate (KH$_2$PO$_4$) buffer solution (pH = 7) with or without 1 M sodium sulfite (Na$_2$SO$_3$). The $\eta_{Injection}$ for H$_2$O was defined as the ratio of photocurrent density of the reaction in H$_2$O (J_{Wat}) to the one obtained in Na$_2$SO$_3$ (J_{Sul}) ($\eta_{injection} = J_{Wat} / J_{Sul}$). The $\eta_{Separation}$ was determined using the equation: $\eta_{Separation} = J_{Sul} / J_{Abs}$, where J_{Abs} is photocurrent density at 100 % internal quantum efficiency.[29]

Electrochemical impedance spectroscopy (EIS) was conducted in the frequency range 10^4 - 0.1 Hz using an amplitude of 20 mV at open circle potential. The impedance *vs.* frequency spectra were acquired at the open circuit potential of the system under light illumination. The measured impedance spectroscopic data were fitted into the models of two RC equivalent circuit with Zsimpwin software. Afterwards,

impedance *vs.* potential data at a fixed frequency (1 KHz) were obtained to determine carrier density. The Mott-Schottky (M-S) plots showing the electron donor density were acquired by using the equation: N_D = (2 / $e\varepsilon\varepsilon_0$) / [d($1 / C^2$) / d$V$], where C is the space charge layers capacitance, e is the electron charge, ε is the dielectric constant, and ε_0 is the permittivity of vacuum.[30]

3. Results and Discussion

As shown in Figure 1, the structural features of Ta-doped TiO_2 nanorods obtained by hydrothermal synthesis at 180 °C were dependent on the hydrothermal time. This is also why the materials were labelled as Ta-PTNA-*t*, where *t* denotes the hydrothermal time. In the initial stage (1 h), sparsely distributed, cube-shaped Ta-doped TiO_2 nanocrystals were epitaxially grow on Ta foil due to their perfect crystalline structures match (Figures 1c and S1a).[24] After *ca.* 5 h, densely grown nanorods, most of which were perpendicularly oriented with respect to the substrate, were observed (Figure 1d). Interestingly, when the reaction time was increased to 10 h, the top of each TiO_2 nanorod gradually dissolved through anisotropic corrosion, forming a hollow opening.[31, 32] The resulting arrays of Ta-doped TiO_2 nanorods, which covered the entire surface of Ta foil, had an average diameter of *ca.* 600 nm (Figure 1e). The cross-sectional image (Figure S2b) showed that Ta-PTNA-10 possessed vertically aligned nanorods with an average length of *ca.* 5.0 µm homogeneously grown on the Ta foil. After 15 h, their diameter increased to 700 nm while their length increased to 5.6 µm (Figure S1d). However, any further increase in hydrothermal time (*e.g.*, to *t* = 24 h) at 180 °C did not cause any significant change in the diameter as well as the length of the nanorods, except making most of the nanorods aggregate (Figures S1e, S2 and S3). Interestingly, when the hydrothermal treatment was performed at 160 °C, nanorods with no hollow opening resulted (Figures S4a and b), and when the synthesis was carried out at 200 °C, most of the nanorods bent down or aggregated (Figures S4c and d). Meanwhile, the undoped TiO_2/FTO had vertically aligned nanorods with no hollow opening (Figure S5). Thus, it can be concluded that Ta plays a major role in the formation of the hollow structure in the nanorods.
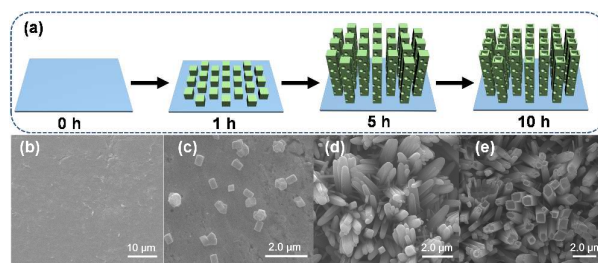

Figure 1. a) Synthetic processes leading to the growth of Ta-doped TiO_2 nanorods arrays on Ta foil by hydrothermal synthesis at 180 °C. SEM images of: b) pristine Ta substrate and hydrothermally-grown TiO_2 arrays on the Ta substrate after the reaction is carried out for c) 1 h, d) 5 h, and e) 10 h.

SEM-based energy-dispersive X-ray spectroscopy (EDX) was conducted on a single nanorod of TiO_2 scraped from the substrate to eliminate the possible impact of the underlying Ta

metal substrate on the analysis. As compiled in Table S2, the results illustrated that the material obtained at 5 h (Ta-PTNA-5) had a large amount of Ta dopant atoms. This must have been due to the fact that in the initial stage of the reaction the rate of Ta doping was much faster than the rate of growth of TiO_2; however, in the later stage the rate of growth of TiO_2 remained the same while the rate of Ta doping into TiO_2 slowed down because the TiO_2 nanorods forming on the surface of the Ta substrate increasingly restricted the dissolution of Ta. Thus, when the reaction time was increased, *e.g.*, to 10 h, a relatively lower amount of Ta dopants made it into the TiO_2 nanorods. Increasing the reaction time further, beyond 10 h, however, made the rate of growth of TiO_2 slower and the relative amount of Ta dopants in TiO_2 concomitantly higher again. Ultimately, 5 h was found to be the optimal hydrothermal time that gives TiO_2 nanorods with the highest Ta-to-TiO_2 ratio.

The XRD patterns of Ta-PTNA materials obtained with different reaction time (Ta-PTNA-10, -15 and -24) all showed more intense (101) peak than (110) peak, indicating the preferential growth of the nanorods along [001] direction (Figure S6). The materials synthesized at 160 and 200 °C and the undoped TiO_2/FTO also appeared to have nanorods mainly grown in a similar direction (Figures S7 and S8). The Rietveld refinement XRD data of Ta-PTNA-10 revealed that the Ta atoms occupying Ti sites were ~1.5 % (Figure S9 and Table S3). XPS survey spectra demonstrated the presence of Ti, Ta, O and C in Ta-PTNA (Figure S10). High-resolution Ti 2p XPS spectra of undoped TiO_2/FTO showed two main peaks, at 458.6 and 464.4 eV, which can be assigned to Ti $2p_{3/2}$ and Ti $2p_{1/2}$ of Ti^{4+}, respectively. However, compared with the Ti 2p peaks of undoped TiO_2, those of Ta-PTNA-*t* shifted slightly to lower banding energies, which is most likely due to the presence of Ta^{5+} dopant species in the TiO_2.[22, 33] The fact that the Ta $4f_{7/2}$ peak being observed at a binding energy of 25.5 eV, which is between that of Ta_2O_5 (25.9 eV) and that of metallic Ta (21.9 eV), is consistent with the incorporation of Ta^{5+} in place of Ti^{4+} in TiO_2 lattice.[34]
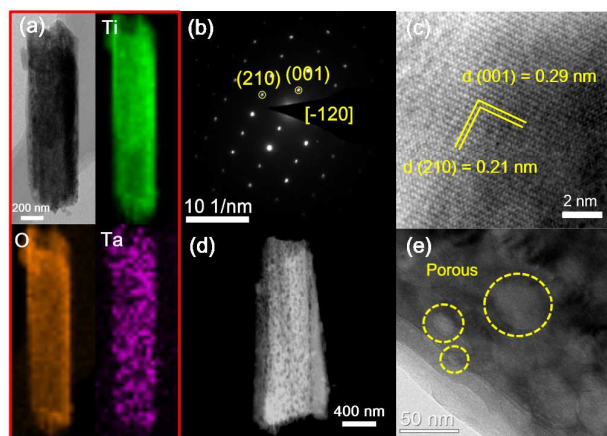
Figure 2. Morphology and structure of Ta-PTNA-10: a) TEM and STEM-EDX images, b) SAED pattern, c) HR-TEM image, d) HAADF image, and d) magnified TEM image.

TEM image and elemental mapping obtained with scanning TEM-based EDX (STEM-EDX) of a single nanorod in Ta-PTNA-10 showed that Ta atoms were present over the entire nanorod

(Figure 2a). The sharp diffraction spots in the selected area electron diffraction (SAED) pattern taken along the zone axis of [-120] (Figure 2b), indexed as the (001) and (210) planes of rutile TiO_2, confirmed the high crystallinity of the material. Furthermore, high resolution TEM (HR-TEM) image (Figure 2c) revealed lattice fringes with interplanar spacings of 0.29 nm and 0.21 nm corresponding to the d-spacing of (001) and (210) crystallographic planes, respectively, of rutile.[26] High angle annular dark field (HAADF) images (Figure 2d) indicated that the Ta-doped TiO_2 nanorod possessed lots of pores with sizes ranging from 10 to 50 nm (Figure 2e). The density and size of pores formed in the nanorods were found to be dependent on hydrothermal reaction time, calcination time and/or calcination temperature. The density of pores decreased as the hydrothermal time was increased from 5 h to 10 h, but then remained about the same afterwards (Figure S11). The pore sizes remained about the same throughout though. While no pores were seen in the nanorods when the calcination temperature was <300 °C (Figure S12), pores were increasingly seen as the temperature was >300 °C. The highest pore density was obtained when the nanorods were synthesized using 450 °C for 1 h (Figure S13), and larger-sized pores, albeit in lower density, were seen in those obtained using higher temperatures (e.g., 550 °C) for 1 h (Figure S12). Meanwhile, only few pores were observed in the nanorods of undoped TiO_2/FTO (Figure S11). These results indicate once again that Ta plays a role in the formation of the pores in the TiO_2 nanorods, most likely through the Kirkendall effect involving ion exchange between Ta^{5+} dopant species and Ti^{4+} ions in the nanorods.[35, 36]
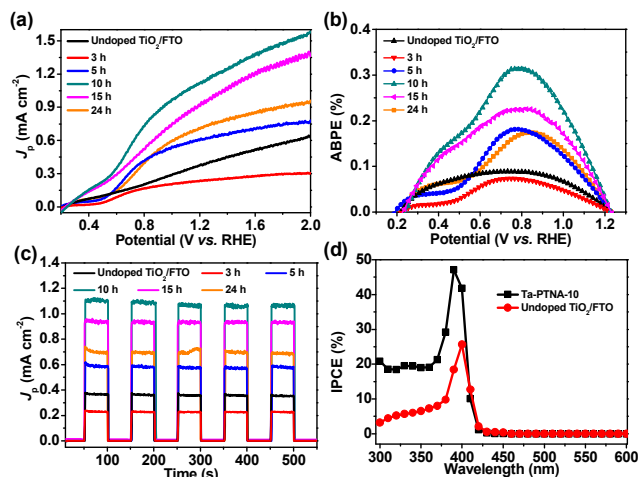
Figure 3. Photoelectrocatalytic performances of Ta-PTNA-*t* and undoped TiO_2/FTO materials for water oxidation: a) plots of photocurrent density vs. applied potential, b) calculated photoconversion efficiency vs. applied potential, c) plots of transient photocurrent density vs. time under simulated sunlight irradiation, and d) IPCE spectra of Ta-PTNA-10 and undoped TiO_2/FTO vs. wavelength of light.

The photoelectrocatalytic activities of Ta-PTNA-*t* materials and the control material (i.e., undoped TiO_2/FTO) for water oxidation were then evaluated. The photocurrent density over Ta-PTNA-*t* materials increased as the calcination time, t, was increased from 3 to 10 h, but then decreased afterwards

ARTICLE

(Figures 3a, S14 and S15a). In other words, the material obtained with t = 10 h (Ta-PTNA-10) showed the best catalytic activity toward the reaction. At an applied potential of 1.23 V (vs. RHE) and without co-catalyst, a high current density of 1.1 mA cm^{-2} was generated with this material, and this is comparable with those obtained with the state-of-the-art TiO_2-based photoanodes and higher than those previously reported for other Ta-doped TiO_2 materials (Table S4).[13, 14, 37-40] Ta-PTNA-3 and Ta-PTNA-5 exhibited lower photocurrent densities of 0.24 and 0.61 mA cm^{-2}, respectively, at the same potential. The relatively lower photocurrent given by these two materials can be accounted by their randomly oriented, smaller density of nanorods (Figures S1b and S1c). Ta-PTNA-15 and Ta-PTNA-24 also gave lower photocurrent densities (0.94 and 0.72 mA cm^{-2}, respectively) than Ta-PTNA-10, though they both gave better photocurrent densities than undoped TiO_2/FTO. Their lower photocurrent density of these two materials compared with that of Ta-PTNA-10 may be the result of their smaller surface area and aggregated nanorods, which give rise to longer diffusion pathways (Figures S1 and S2).[14, 41] The Ta-PTNA materials obtained at hydrothermal temperatures of 160 and 200 °C also showed lower current density compared with Ta-PTNA-10. These two materials have lower crystallinity and aggregated structure, respectively, due to the respective lower (160 °C) and higher (200 °C) hydrothermal temperatures used to synthesize them (Figures S4, S7 and S15b). Ta-PTNA-10 obtained using 450 °C as calcination temperature exhibited the best catalytic performance than the corresponding materials obtained using lower and higher calcination temperatures (Figure S15c); this is because the nanorods obtained at lower temperatures (below ca. 400 °C) had less pore density and those obtained at higher temperatures (above ca. 500 °C) peeled off from the substrate or were unstable (Figure S16).

The applied bias photon-to-current efficiency (ABPE, %) as a function of the applied potential (Figure 3b) revealed that Ta-PTNA-10 gave the highest efficiency, with a value of 0.32 % at 0.79 V, which is ~4 times higher than that of undoped TiO_2/FTO (0.08 %). Ta-PTNA-5, Ta-PTNA-15 and Ta-PTNA-24 also afforded optimal ABPE efficiencies of 0.18 %, 0.22 % and 0.17 % at an applied bias of 0.79 V, respectively. Amperometric I-t curves measured at 1.23 V under chopped light irradiation over the materials displayed nearly vertical rise and fall in the values of current densities (Figure 3c). This indicated that the charge transport in the photoelectrodes occurred quickly in the direct electron transfer pathway provided by the nanorods in Ta-PTNA materials.[10] Moreover, no significant loss of current density was observed after 10 h of reaction under light (Figure S17a). In addition, the H_2 production rate is ~15.9 μmol/h at an applied bias of 1.23 V vs. RHE under AM 1.5G illumination (Figure S17b). Abundant of bubbles was observed at both photoanode and cathode (Figure S17c, d), suggesting the photocurrent increase after irradiation merely come from the splitting of water but not some other reactions on photoanode.[42] Figure 3a shows the collected gas volume as a function of time.Furthermore, the maximum incident photon-to-current conversion efficiencies (IPCE) over Ta-PTNA-10 photoelectrode at incident light of 390 nm was found to be 48 % whereas the corresponding value over undoped TiO_2/FTO photoelectrode was only ca. 25 % (Figure 3d). This means, charge carrier separation and transport were more effective in Ta-TNRAs-10 than in the undoped TiO_2 nanorods.

To get a deeper understanding of the reasons behind higher photocurrent density, three possible fundamental processes taking place during photoelectrocatalysis were systemically investigated by taking into consideration the following equation, Equation (1):[29]

$$J_P = J_{Abs} \times \eta_{Injection} \times \eta_{Separation} \tag{1}$$

Where J_P is the measured photocurrent density for water oxidation, J_{Abs} is the photocurrent density at 100 % internal quantum efficiency, $\eta_{Injection}$ is the efficiency of involvement of surface-reaching holes in water oxidation, and $\eta_{Separation}$ is the photogenerated electron-hole separation efficiency. UV-Vis spectra clearly showed that the largest absorbance between 300 to 420 nm was shown by Ta-PTNA-10, followed by Ta-PTNA-15 and then Ta-PTNA-24 (Figure 4a and Figure 4b), a result that is well in line with their PEC performances. This is in accordance with their porous and hollow-opening in their 1-D structure, which must have allowed multiple reflections of light to occur in these materials (Figure 4a and S21).[43] (Note that the absorbance between 420 - 600 nm (Figures S18, S19 and S20) was mainly due to Ta foil, which does not directly contribute to Ta-PTNAs' photocatalytic activity). Besides, all the Ta-PTNA materials showed higher $\eta_{Injection}$ than undoped TiO_2/FTO (~80 % at 1.23 V (vs. RHE)). Most notably, Ta-PTNA-10 photoelectrode gave $\eta_{Injection}$ of 98 % (Figures 4c and S22). This high value of $\eta_{Injection}$ is most likely due to the porous structures in the nanorods of this material, which allow electrolyte to easily reach its catalytic sites and the photogenerated holes to have short diffusion pathways over the material.[28, 44] However, compared with the value of $\eta_{Injection}$ of undoped TiO_2/FTO at 1.23 V (vs. RHE), that of Ta-PTNA-10 was only 1.25 times higher and not large enough to explain its ~3 times higher catalytic performance. The additional factor must have been the favorable charge separation observed in Ta-PTNA-10 by experiments. Ta-PTNA-10 showed higher $\eta_{Separation}$ (= J_{Sul}/J_{Abs}, where J_{Sul} is the measured photocurrent density for sulphite oxidation) of 60 % at 1.23 V vs. RHE (Figures 4d, S21 and S23), which is larger than those of other Ta-PTNA materials and 2.4 times as high as that of undoped TiO_2/FTO (25 %). Based on these results, it can be concluded that Ta-PTNAs' structure significantly inhibits charge recombination and facilitates the consumption of photogenerated holes during photoelectrocatalysis (Figure 4a).
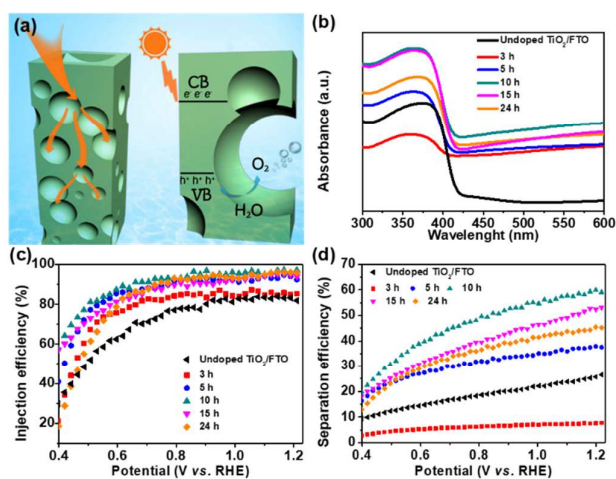
Figure 4. a) Schematic illustration of multiple reflections of light in a porous Ta-PTNA nanorod and subsequent charge separation and charge transport processes in it. b) UV-Vis absorbance spectra, c) calculated charge injection efficiency, and d) charge separation efficiency for Ta-PTNA-*t* and undoped TiO_2/FTO photoanodes.

In the Mott-Schottky (M-S) plots (Figure 5a), Ta-PTNA-10 photoelectrode exhibited the smallest slope and gave the highest calculated donor density (2.87×10^{18} cm^{-3}) among all of the Ta-PTNA materials (Table S5).[45] It is worth mentioning that direct comparison of M-S slopes and donor densities of Ta-PTNA-10 and undoped TiO_2/FTO may not be precise due to the different underlying substrates in them, *i.e.*, Ta foil versus FTO (Figures 5b and Figure S24). To get around this issue, the Ta-PTNA-10 nanorods were scraped off of Ta foil and then coated on FTO (Figure 5c). This electrode showed smaller M-S slope and larger donor density than the scraped undoped TiO_2/FTO. This result suggested that the Ta doping in TiO_2 nanoarrays resulted in higher electron density and electronic conductivity (see Figure S24 for more detailed explanation).
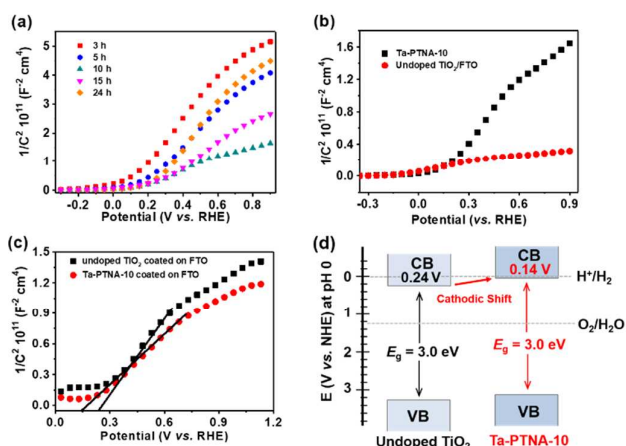

Figure 5. M-S plots collected at 1 kHz in the dark of: a) different Ta-PTNA-t photoanode materials, b) Ta-PTNA-10 and undoped TiO_2/FTO photoanodes, c) scraped undoped TiO_2 powder and scraped Ta-PTNA-10 powder that are coated on FTO. d) Potential energy diagrams of undoped TiO_2/FTO and Ta-PTNA-10.

By taking the *x* intercept of linear fit in the M-S plots, the flat band potential (E_{FB}) can be obtained. Depicted in Figure 5c are the E_{FB} of the undoped TiO_2/FTO and Ta-PTNA-10 was 0.24 V and 0.14 V (*vs.* RHE), respectively. Assuming the gap between flat band potential and bottom edge of conduction band can be negligible for n-type semiconductors, the potential energy diagram (Figure 5d) were determined by the E_{FB} and the optical band gap energies (Tauc plot).[46-48] The results suggest that Ta doping makes both the flat band and the conduction band potential undergo a cathodic shift with a value of 0.1 V. This negative shift in the flat band potential is not only favorable for inhibition of potogenerated hole-electron recombination but also beneficial for the material to find practical application as electrode to generate H_2 from water. [48, 49]

The EIS spectra of all the materials (Figure 6) showed Nyquist plots consisting of two semicircles in the high to low

frequency regions, corresponding to the resistance of electron transport within the electrode and at the electrode/electrolyte interface, respectively.[50] The equivalent circuits depicted in Figure S25 were employed to fit the EIS data to obtain the optimum fitting values (Tables S6 – S10). The arches for Ta-PTNA-10 were much smaller than those for all the control materials (Figures 6 and S26), especially undoped TiO_2/FTO, confirming again that Ta doping gave rise to faster charge carrier transport and lower resistance in the electrode. It is worth adding that the semicircles related with the electron transport within electrodes under dark are much larger than those under illumination in both cases (Ta-PTNA-10 and undoped TiO_2/FTO) (Figure 26a), demonstrating that the photogenerated charge carriers substantially reduced the charge-transfer resistance. The larger resistance was obtained for the materials obtained by calcination at <400 °C or at >500 °C (Figure 6b), likely because of their low pore density and greater tendency to peel off from the underlying substrate, respectively. On the contrary, owing to its large surface area, Ta-PTNA-10 exhibited greater interfacial charge transfer rate between itself and the electrolyte and substantially lower electron-hole recombination rate[51, 52] To further investigated the photogenerated carrier transfer behavior of Ta-PTNA-10 and the undoped TiO_2 materials, photoluminescence (PL) spectroscopy (Figure S27a) was conducted at room temperature. The PL intensity at 410 nm of Ta-PTNA-10 is lower than that of the undoped material, indicating Ta doping has significantly suppressed the recombination of photogenerated charge carriers.[53] Moreover, the fluorescence lifetime values, calculated from the time resolved PL spectroscopy (Figure S27b), are 0.54 and 0.68 ns for undoped TiO_2 and Ta-PTNA-10, respectively. The prolonged fluorescence lifetime of Ta-PTNA-10 is related to a long life of electrons in the excited state, which can enhance the charge separation efficiency and retard charge recombination, and thus giving better performance for photoelectrocatalytic water oxidation. [54, 55]
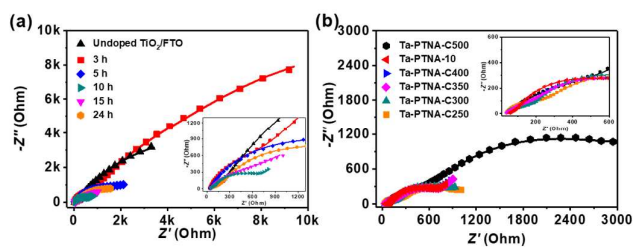
Figure 6. a) Nyquist plots (and magnified Nyquist plots in inset), with experimental data and simulated responses denoted by discrete points and solid lines, respectively, for Ta-PTNA-*t* and undoped TiO_2/FTO photoanodes. b) Nyquist plots of Ta-doped porous TiO_2 nanorods obtained at different calcination temperatures for 1 h. The experimental data and simulated impedance response are represented by discrete points and solid lines, respectively.

4. Conclusions

In conclusion, Ta-doped porous TiO_2 nanorods arrays (Ta-PTNAs) have been successfully synthesized *via* a simple, template-free synthetic route. The porous structure in the

ARTICLE

nanorods arrays is believed to have formed by Ta-assisted Kirkendall effect. Compared with undoped TiO_2/FTO and many other previously reported photocatalysts, Ta-PTNA photoanodes showed much higher PEC catalytic activity toward water oxidation. Ta-PTNAs' excellent photocatalytic activity has been attributed to their Ta dopants, large porosity and 1-D structure, and the low charge recombination rate on them. The reported Ta-PTNA materials can thus become promising photoelectrodes for a variety of solar energy-based applications such as solar cells, besides photoelectrocatalytic water.

Conflicts of interest

There are no conflicts to declare.

Acknowledgements

Notes and references

1. W. J. Youngblood, S.-H. A. Lee, Y. Kobayashi, E. A. Hernandez-Pagan, P. G. Hoertz, T. A. Moore, A. L. Moore, D. Gust and T. E. Mallouk, *J. Am. Chem. Soc.*, 2009, **131**, 926-927.
2. P. Xu, N. S. McCool and T. E. Mallouk, *Nano Today*, 2017, **14**, 42-58.
3. Y. Meng, D. Voiry, A. Goswami, X. Zou, X. Huang, M. Chhowalla, Z. Liu and T. Asefa, *J. Am. Chem. Soc.*, 2014, **136**, 13554-13557.
4. M. G. Walter, E. L. Warren, J. R. McKone, S. W. Boettcher, Q. Mi, E. A. Santori and N. S. Lewis, *Chem. Rev.*, 2010, **110**, 6446-6473.
5. J. S. Luo, J. H. Im, M. T. Mayer, M. Schreier, M. K. Nazeeruddin, N. G. Park, S. D. Tilley, H. J. Fan and M. Grätzel, *Science*, 2014, **345**, 1593-1596.
6. A. Fujishima and K. Honda, *Nature*, 1972, **238**, 37-38.
7. E. Hendry, M. Koeberg, B. O'Regan and M. Bonn, *Nano Lett.*, 2006, **6**, 755-759.
8. T. Tachikawa, S. Yamashita and T. Majima, *J. Am. Chem. Soc.*, 2011, **133**, 7197-7204.
9. M. Xu, P. M. Da, H. Y. Wu, D. Y. Zhao and G. F. Zheng, *Nano Lett.*, 2012, **12**, 1503-1508.
10. G. J. Ai, H. X. Li, S. P. Liu, R. Mo and J. X. Zhong, *Adv. Funct. Mater.*, 2015, **25**, 5706-5713.
11. M. Ge, Q. Li, C. Cao, J. Huang, S. Li, S. Zhang, Z. Chen, K. Zhang, S. S. Al-Deyab and Y. Lai, *Adv. Sci.*, 2017, **4**, 1600152-1600182.

12. M. Wang, J. Ioccozia, L. Sun, C. Lin and Z. Lin, *Energy Environ. Sci.*, 2014, **7**, 2182-2202.
13. I. S. Cho, Z. B. Chen, A. J. Forman, D. R. Kim, P. M. Rao, T. F. Jaramillo and X. L. Zheng, *Nano Lett.*, 2011, **11**, 4978-4984.
14. Y. J. Hwang, C. Hahn, B. Liu and P. D. Yang, *ACS Nano*, 2012, **6**, 5060-5069.
15. H. A. Park, S. Liu, Y. Oh, P. A. Salvador, G. S. Rohrer and M. F. Islam, *ACS Nano*, 2017, **11**, 2150-2159.
16. J. Zhao, T. Minegishi, L. Zhang, M. Zhong, Gunawan, M. Nakabayashi, G. J. Ma, T. Hisatomi, M. Katayama, S. Ikeda, N. Shibata, T. Yamada and K. Domen, *Angew. Chem. Int. Ed.*, 2014, **53**, 11808-11812.
17. Q. Wei, F. Xiong, S. Tan, L. Huang, E. H. Lan, B. Dunn and L. Mai, *Adv. Mater.*, 2017, **29**, 1602300-1160238.
18. Y. Hou, Z. Wen, S. Cui, X. Feng and J. Chen, *Nano Lett.*, 2016, **16**, 2268-2277.
19. L. R. Sheppard, S. Hager, J. Holik, R. Liu, S. Macartney and R. Wuhrer, *J. Phys. Chem. C*, 2015, **119**, 392-400.
20. X. J. Feng, K. Shankar, M. Paulose and C. A. Grimes, *Angew. Chem. Int. Ed.*, 2009, **48**, 8095-8098.
21. M. M. Momeni and Y. Ghayeb, *J. Electroanal. Chem.*, 2015, **751**, 43-48.
22. Y. Yan, J. Lee and X. Cui, *Vacuum*, 2017, **138**, 30-38.
23. C. Das, P. Roy, M. Yang, H. Jha and P. Schmuki, *Nanoscale*, 2011, **3**, 3094-3096.
24. X. F. Yang, J. Chen, L. Gong, M. M. Wu and J. C. Yu, *J. Am. Chem. Soc.*, 2009, **131**, 12048-12049.
25. S. Hoang, S. W. Guo and C. B. Mullins, *J. Phys. Chem. C*, 2012, **116**, 23283-23290.
26. G. M. Wang, H. Y. Wang, Y. C. Ling, Y. C. Tang, X. Y. Yang, R. C. Fitzmorris, C. C. Wang, J. Z. Zhang and Y. Li, *Nano Lett.*, 2011, **11**, 3026-3033.
27. Y. Hou, F. Zuo, A. Dagg and P. Y. Feng, *Angew. Chem. Int. Ed.*, 2013, **52**, 1248-1252.
28. X. J. Shi, Y. Choi, K. Zhang, J. Kwon, D. Y. Kim, J. K. Lee, S. H. Oh, J. K. Kim and J. H. Park, *Nat. Commun.*, 2014, **5**, 4775-4782.
29. T. W. Kim and K. S. Choi, *Science*, 2014, **343**, 990-994.
30. Z. H. Zhang and P. Wang, *Energy Environ. Sci.*, 2012, **5**, 6506-6512.
31. M. Wang, D. Zheng, M. Ye, C. Zhang, B. Xu, C. Lin, L. Sun and Z. Lin, *Small*, 2015, **11**, 1436-1442.
32. L. Liu, J. Qian, B. Li, Y. Cui, X. Zhou, X. Guo and W. Ding, *Chem. Commun.*, 2010, **46**, 2402-2404.
33. S. M. Bawaked, S. Sathasivam, D. S. Bhachu, N. Chadwick, A. Y. Obaid, S. Al-Thabaiti, S. N. Basahel, C. J. Carmalt and I. P. Parkin, *J. Mater. Chem. A*, 2014, **2**, 12849-12856.
34. X. Zhang, H. Li, S. Wang, F.-R. F. Fan and A. J. Bard, *J. Phys. Chem. C*, 2014, **118**, 16842-16850.
35. J. Liu, Y. Amit, Y. Li, A. M. Plonka, S. Ghose, L. Zhang, E. A. Stach, U. Banin and A. I. Frenkel, *Chem Mater*, 2016, **28**, 8032-8043.
36. X. S. Nguyen, G. Zhang and X. Yang, *ACS Appl. Mater. Interfaces*, 2017, **9**, 8900-8909.
37. C. Y. Mao, F. Zuo, Y. Hou, X. H. Bu and P. Y. Feng, *Angew. Chem. Int. Ed.*, 2014, **53**, 10485-10489.
38. A. Li, Z. Wang, H. Yin, S. Wang, P. Yan, B. Huang, X. Wang, R. Li, X. Zong, H. Han and C. Li, *Chem. Sci.*, 2016, **7**, 6076-6082.
39. Y. Mi, L. Wen, R. Xu, Z. Wang, D. Cao, Y. Fang and Y. Lei, *Adv. Energy Mater.*, 2016, **6**, 1501496-1501503.
40. M. Altomare, K. Lee, M. S. Killian, E. Selli and P. Schmuki, *Chem.-Eur. J.*, 2013, **19**, 5841-5844.
41. Z. Xie, X. X. Liu, W. P. Wang, X. J. Wang, C. Liu, Q. Xie, Z. C. Li and Z. J. Zhang, *Nano Energy*, 2015, **11**, 400-408.

42. P. L. Yan, G. J. Liu, C. M. Ding, H. X. Han, J. Y. Shi, Y. Gan and C. Li, *ACS Appl. Mater. Interfaces*, 2015, **7**, 3791-3796.
43. C. Li, A. Li, Z. Luo, J. Zhang, X. Chang, Z. Huang, T. Wang and J. Gong, *Angew. Chem. Int. Ed.*, 2017, **129**, 4214-4219.
44. W. Yang, Y. Yu, M. B. Starr, X. Yin, Z. Li, A. Kvit, S. Wang, P. Zhao and X. Wang, *Nano Lett.*, 2015, **15**, 7574-7580.
45. Y. C. Wang, Y. Y. Zhang, J. Tang, H. Y. Wu, M. Xu, Z. Peng, X. G. Gong and G. F. Zheng, *ACS Nano*, 2013, **7**, 9375-9383.
46. J. Resasco, H. Zhang, N. Kornienko, N. Becknell, H. Lee, J. Guo, A. L. Briseno and P. Yang, *ACS Cent. Sci.*, 2016, **2**, 80-88.
47. C. Z. Wang, Z. Chen, H. B. Jin, C. B. Cao, J. B. Li and Z. T. Mi, *J. Mater. Chem. A*, 2014, **2**, 17820-17827.
48. S. J. Hong, S. Lee, J. S. Jang and J. S. Lee, *Energy Environ. Sci.*, 2011, **4**, 1781-1787.
49. J. T. Li, M. W. G. Hoffmann, H. Shen, C. Fabrega, J. D. Prades, T. Andreu, F. Hernandez-Ramirez and S. Mathur, *J Mater. Chem.*, 2012, **22**, 20472-20476.
50. J. G. Hou, C. Yang, H. J. Cheng, S. Q. Jiao, O. Takeda and H. M. Zhu, *Energy Environ. Sci.*, 2014, **7**, 3758-3768.
51. M. F. Shao, F. Y. Ning, M. Wei, D. G. Evans and X. Duan, *Adv. Funct. Mater.*, 2014, **24**, 580-586.
52. Y. Hou, F. Zuo, A. P. Dagg, J. K. Liu and P. Y. Feng, *Adv. Mater.*, 2014, **26**, 5043-5049.
53. W. Chen, T. Wang, J. Xue, S. Li, Z. Wang and S. Sun, *Small*, 2017, **13**, 1602420-1602427.
54. X. Wu, J. Zhao, S. Guo, L. Wang, W. Shi, H. Huang, Y. Liu and Z. Kang, *Nanoscale*, 2016, **8**, 17314-17321.
55. F. Ning, M. Shao, S. Xu, Y. Fu, R. Zhang, M. Wei, D. G. Evans and X. Duan, *Energy Environ. Sci.*, 2016, **9**, 2633-2643.

Table of Content (ToC) Figure